Experiments in Fluids (2006) 41: 309–318
DOI 10.1007/s00348-006-0145-6

RESEARCH ARTICLE

W. Zhu · R. van Hout · L. Luznik · H. S. Kang
J. Katz · C. Meneveau

A comparison of PIV measurements of canopy turbulence performed in the field and in a wind tunnel model

Received: 16 November 2005 / Revised: 6 March 2006 / Accepted: 27 March 2006 / Published online: 5 May 2006
© Springer-Verlag 2006

Abstract Particle image velocimetry (PIV) has been used to compare between turbulence characteristics just within and above a mature corn canopy and those of a model canopy setup in a wind tunnel (WT). The laboratory normalized mean velocity profile is adjusted using variable mesh screens to match the normalized mean shear of the corn field (CF) data. The smallest resolved scale in the field is about 15 times the Kolmogorov length scale ($\eta_{CF} \approx 0.4$ mm), whereas in the WT it is 5 times η_{WT} ($\eta_{WT} \approx 0.15$ mm). In both cases, the mean velocity and turbulence statistics are consistent with those measured using single point sensors. However, the profiles of normalized Reynolds shear stress in the field and the laboratory differ. Turbulent spectral densities calculated from PIV spatial and time series in the field display an inertial range spanning three decades. In the laboratory due to lower Reynolds numbers, the inertial range shrinks to two decades. Quadrant-Hole analysis is applied to Reynolds shear stress, vorticity magnitude and dissipation rates. In quadrants 1–3, the WT and field conditionally sampled stresses show similar trends. However, a conflicting trend is found in the sweep quadrant. The analysis confirms that sweep and ejections dominate the momentum flux and dissipation rate.

The content of this paper, entitled "Applying PIV for Measuring Turbulence just within and above a Corn Canopy," was presented at the 6th International Symposium on Particle Image Velocimetry at Pasadena, CA, USA, September 21–23, 2005.

W. Zhu · R. van Hout · L. Luznik · H. S. Kang · J. Katz (✉)
C. Meneveau
Department of Mechanical Engineering,
The Johns Hopkins University, 3400 N. Charles Street,
Baltimore, MD 21218, USA
E-mail: katz@poseidon.me.jhu.edu
Tel.: +1-410-5165470
Fax: +1-410-5167254

1 Introduction

Understanding of the mean flow and turbulence structure as well as associated transport processes that occur within and above plant canopies is essential to improve the modeling of pollen dispersal, chemical exchanges, and momentum and energy fluxes between air and canopy. In the last three decades, extensive measurements inside and above canopies have been performed using single point sensors, e.g., hotwire and hot-film anemometer, laser Doppler velocimetry and sonic anemometers (see, among others, Brunet et al. 1994; Shaw et al. 1974a, b; Wilson et al. 1982; Poggi et al. 2004). Normalized streamwise mean velocity profiles exhibit an inflection point at canopy height for a wide range of rough boundaries, both in wind tunnel (WT) and field experiments. This distinct feature and other properties of canopy flows suggest an analogy to mixing layers (Raupach et al. 1991; Finnigan 2000). The structure of the Reynolds stress and its dependence on the Projected Frontal Area Index (PFAI) was investigated by Raupach (1981) who performed Quadrant-Hole (Q-H) analysis using WT, x-wire anemometer data. He observed that the stress fraction difference between sweeps and ejections increased with increasing PFAI near canopy height, and became insensitive to the roughness at higher elevations. Shaw et al. (1983) conducted hot-film anemometer measurements in a mature corn field (CF), and also performed Q-H analysis. They claimed that their results were similar to those of Raupach (1981) in the sense that extreme events contributed significantly to the average Reynolds stress. In this paper, we take advantage of particle image velocimetry (PIV), and extend the Q-H analysis to the transverse vorticity component and dissipation rate.

We combine and compare field measurements just within and above a mature corn canopy with WT measurements over and inside a model canopy. In the field, the large-scale structures are resolved by invoking Taylor's hypothesis on the PIV time series, whereas the

small scales are resolved directly from the vector maps. In both studies, the PIV measurements are compared and found to agree with single point data, i.e., to a 3D Campbell Sonic Anemometer/Thermometer (CSAT) in the field, and to a hotwire anemometer (streamwise velocity component only) in the WT.

The normalized vertical profiles of mean velocity in the tunnel are made to agree with the field data using screens with variable mesh sizes. The turbulence characteristics are compared, showing some discrepancies in trends with elevation. The normalized turbulent kinetic energy spectra of the field and laboratory data sets collapse except for effects of noise. As in previous studies, Q-H analysis confirms that sweeps and ejections are the main contributors to momentum transfer. Stress fraction values in the WT are lower than those in the CF, while for sweeps the trends with height are reversed. Taking advantage of the spatial information of PIV, we also perform Q-H analysis on vorticity magnitude and dissipation rate, which have similar trends.

2 Description of the field and wind tunnel experiments

2.1 Field experiments

The field PIV measurements were performed on 22 July 2003, from 0030 EDT to 0330 EDT, within a flat, irrigated, 400 m radius, half circular, fully matured CF, located on the eastern shore of the Chesapeake Bay, MD, USA. The roughness of the CF was characterized by a leaf area index, LAI = 6 ± 0.6, and a PFAI = 3.7 ± 0.5. Details on how these variables were calculated for the field measurements are provided in R. van Hout et al. (submitted for publication). The system was positioned 100 m south of the center of the field, 5.3 m inside the CF. The laser sheet forming optics and CCD camera (DALSA, 12 bit, 2,048 × 2,048 pixels) were mounted on a retractable, rotating platform that could be raised up to 9.75 m above the ground (Fig. 1a). A flashlamp pumped dye laser and PIV acquisition/control computers were housed in a truck, and the light was fed via optical fibers to the platform where the beam was expanded to a 3 mm thick sheet. Further descriptions of the platform as it was deployed in the field and in the ocean are provided in R. van Hout et al. (submitted for publication) and Nimmo Smith et al. (2002, 2005). The plane of the sheet was aligned with the wind direction using a wind vane. The camera's field of view was 18.2 × 18.2 cm^2. Oil-based fog was used as flow tracer. The test site was seeded by slowly releasing the fog through 10 cm diameter perforated pipes that were laid out just below canopy height in a half circle with radius of about 30 m around the measurement system (Fig. 1b).

Measurements were conducted at four different heights, z/h = 1.29, 1.20, 1.11 and 0.97, where z is the height of the center of the field of view measured from the ground, and h = 2.67 m is the average canopy height around the system. At each elevation, 4,096 double-exposure images were acquired at a rate of 4 Hz. The PIV images were processed using interrogation windows of 64 × 64 pixels (5.6 × 5.6 mm^2), with 50% overlap between windows. The resulting instantaneous velocity distributions contain 64 × 64 vectors with a spacing of 2.8 mm. In-house developed correlation software (Roth and Katz 1999, 2001) was used for analyzing the data. The uncertainty in the measurements was about 0.2 pixels (0.06 m/s), provided there was sufficient seeding. Since the seeding particles were not always uniformly distributed, we discarded vectors that did not satisfy a minimum correlation coefficient, and subsequently utilized only those maps that contained 70% or more vectors. The number of vector maps passing our criteria at each elevation was 3,300 ± 100. An instantaneous velocity map superimposed with the vorticity distribution is shown in Fig. 2a.

2.2 Wind tunnel experiments

Particle image velocimetry measurements of the flow inside and over a model canopy were performed in the Corrsin WT (closed-loop) at The Johns Hopkins University. A schematic layout of the experimental setup is shown in Fig. 1c. The WT had a 10 m long test section with a cross-sectional area of 1.2 × 0.91 m^2 (Kang et al. 2003). It was not equipped with an adjustable roof plate as is generally the case in modeling of atmospheric boundary flows (e.g., Brunet et al. 1994), resulting in a pressure drop along the test section. The turbulence level was enhanced by an active grid (Kang et al. 2003), placed 1.2 m upstream of a shear generator that was located 1 m upstream of the start of the model canopy. The shear generator consisted of 17 strips of mesh wire (5 × 91 cm^2) with varying mesh size (Fig. 3; Table 1) that were mounted on a metal frame attached to the interior walls of the WT. It was designed to create the same normalized mean velocity profile as the one obtained in the field experiments by adjusting the mesh size.

The model canopy filled the whole test section in the spanwise direction over a streamwise length of 4.6 m. It consisted of 30 cm long wooden sticks (diameter d = 3.2 mm), that were inserted in 5 cm thick styrofoam in a staggered configuration (see Fig. 1d). In order to prevent upstream flow separation, the height of the styrofoam base was slowly increased at an angle of 6.5° to its full thickness. The height of the model canopy was h = 25 cm, with an average occupied area per canopy element A = 7.26 cm^2. The PFAI equaled $hd/A \approx 1$, and the corresponding frontal area per unit volume equaled ~4.14 m^2/m^3. Note, this configuration was very close to the densest setup (4.27 m^2/m^3) of Poggi et al. (2004) but much sparser than that in the CF, where PFAI ≈ 3.7. The consequences of this difference will be discussed in Sect. 3.

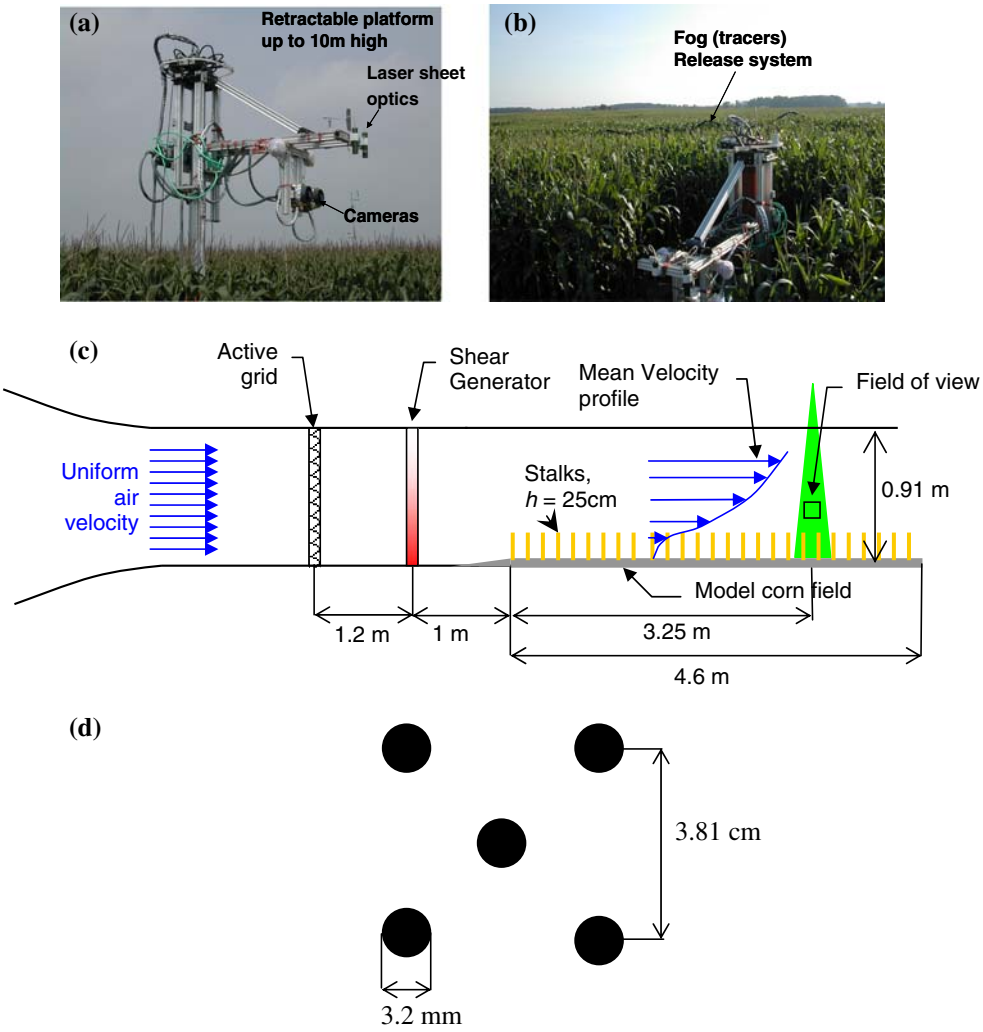

Fig. 1 **a** Particle image velocimetry platform in field experiment, **b** seeding system, **c** wind tunnel setup (not to scale), **d** configuration of model

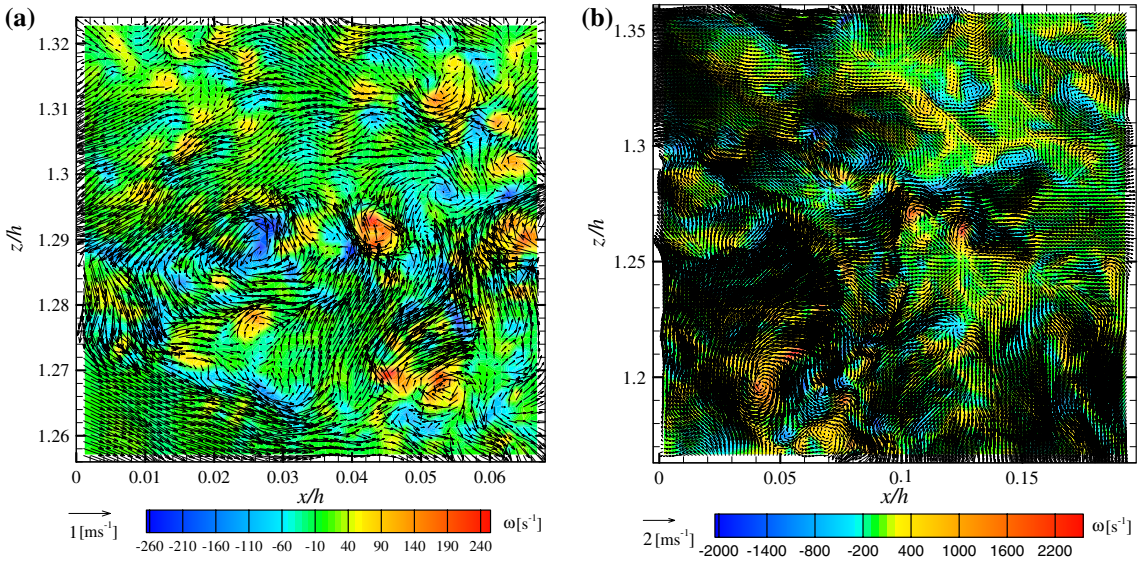

Fig. 2 Vector maps of the instantaneous velocity field superimposed on the vorticity distribution. The instantaneous spatial mean velocity is subtracted to highlight the flow structure. **a** Corn field—spatial mean velocity removed: (1.73,1.47) (m/s), **b** wind tunnel—spatial mean velocity removed: (6.52,0.11) (m/s)

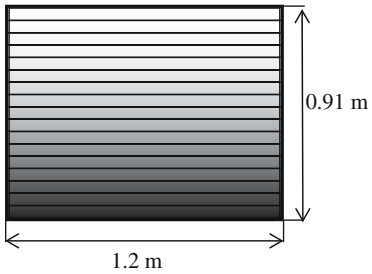

Fig. 3 Shear generator setup. Grayscales give an indication of the mesh size. Exact mesh sizes are given in Table 1

Table 1 Mesh sizes of the shear generator screen

Row # Top to bottom	Mesh size (gaps/in.)
1, 2	Open
3, 4	4
5, 6	8
7, 8	14
9, 10	16
11, 12	20
13, 14	30
15, 16	40
17	Solid

The PIV setup comprised one cross-correlation CCD camera (2kx2k, Kodak ES4.0, 8 bit), and an Nd:Yag laser (120 mJ/pulse, New-Wave Research). A vertical light sheet with thickness of ~1 mm was generated at the centerline of the WT, aligned in the streamwise direction and centered between two rows of canopy elements. The field of view was 4.86×4.86 cm^2, located 3.25 m downstream of the start of the canopy. Measurements were performed at elevations ranging between $z/h = 0.81$ and 2.13 in steps of ~0.17 resulting in an overlap of about 0.5–1 cm between successive elevations. Optical access below the canopy was achieved by removing one row of sticks in the spanwise direction. We verified that removing these few sticks had very little effect on the velocity distribution. PIV data was acquired at a rate of 5 Hz. For each elevation, 40 runs were acquired, each run containing 59 cross-correlation image pairs, resulting in a total of 2,360 PIV image pairs. There was an interval of about 5 min between adjacent runs to save the data to hard disk. During a change in elevation, the WT was shut down and the light sheet was adjusted. For all the measurements, the mean velocity at the canopy height was held at about 3.17 m/s, with a maximum deviation of 1.5%. The WT PIV images were processed using 32×32 pixel interrogation windows with 50% overlap resulting in a vector spacing of 0.380 mm. The remaining sticks near the edges of the images were masked during data processing to avoid spurious data. Figure 2b shows a sample of an instantaneous velocity map above canopy height.

For both the CF and the WT data sets, the 2D vector maps were used to calculate the ensemble averaged velocity profiles, turbulence characteristics, vorticity and spatial energy spectra. Second order finite differencing was used for calculating spatial derivatives. In the results that follow, U is the mean streamwise velocity. x_i, i.e., $x_1 = x$, $x_2 = y$, $x_3 = z$, are the streamwise, spanwise and wall-normal direction, respectively. u_i is the fluctuating component and σ_i is the rms value of the fluctuating component along x_i, where $i = 1, 2, 3$. Spatial and ensemble averaging is indicated by $\langle .. \rangle$.

3 Experimental results

3.1 Mean and turbulent statistics

Vertical profiles of mean streamwise velocity and turbulence statistics measured in the CF and the WT are compared in Fig. 4. In addition to the PIV data, for the WT we also provide hotwire data of the streamwise velocity component. The data sets are normalized by the mean velocity at canopy height, U_h, and the friction velocity, u_*. For the field data, the normalizing velocities and friction velocities are measured at the same times as the PIV field experiments, using a CSAT located at canopy height, about 20 m from the PIV system. The friction velocity is calculated using $u_* = (\langle u_1 u_3 \rangle^2 + \langle u_2 u_3 \rangle^2)^{1/4}$ (Jacobson 1999) at canopy height since the CSAT is not aligned with the main wind direction. In the WT, the friction velocity, is determined from the PIV data, as the square root of the Reynolds shear stress, $\langle -u_1 u_3 \rangle$, at canopy height (Finnigan 2000). It is used to normalize both the hotwire and the PIV results. The mean velocity profiles of the WT measurements, $U(z)$, have slight variations between intentionally overlapping ranges of data sets obtained at adjacent elevations. These variations are most likely a result of slight differences in WT air velocity between measurements performed at different times and elevations. The value of U_h is chosen based on the case that covers $z/h = 1.0$ (yielding $U_h = 3.17$ m/s). The normalized data at other elevations are adjusted to make the transitions match when plotted as $U(z)/U_h$. The variations in the normalizing U_h are less than 1.5% (e.g., $U_h = 3.125$ m/s at measurement station $z/h = 1.61$; $U_h = 3.216$ m/s at $z/h = 0.81$).

Figure 4a shows the corrected values. A similar procedure has been applied to the normalized Reynolds stress profiles shown in Fig. 4b, by adjusting the friction velocity. In this case, the maximum correction is 5%, but typical values are 1–3%, e.g., at measurement station $z/h = 1.0$, $u_* = 0.913$ m/s; $z/h = 1.61$, $u_* = 0.890$ m/s; $z/h = 2.13$, $u_* = 0.960$ m/s. The WT hotwire and PIV data sets compare well with some small differences at low and high elevations. Also, there is very little difference between the normalized field and WT velocity profiles, as enforced by the shear generator. Moreover, the mean velocity profile in WT is only slightly steeper than that of Poggi et al. (2004). For example, at $z/h = 1.5$, our velocity is $U/U_h = 1.7$, while theirs is $U/U_h \sim 1.5$. As expected for canopy flows (Finnigan

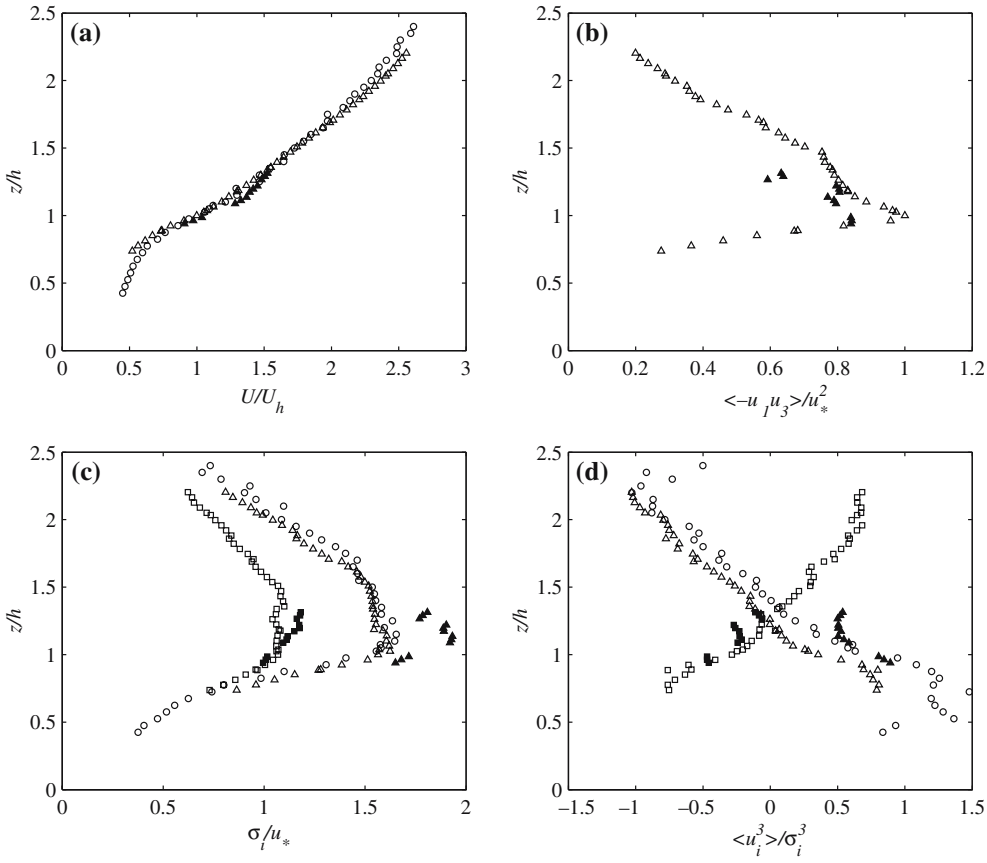

Fig. 4 Mean flow and turbulence statistics of the field and wind tunnel (WT) model canopy flow. ○ Hotwire anemometer data, △ PIV–WT (in Fig. (**c**), and (**d**), u_1 component), □ PIV–WT (in Fig. (**c**), (**d**), u_3 component). Closed symbols PIV-CF

2000), an inflection point is observed at canopy level. The shear stress, $\langle -u_1u_3\rangle$, is plotted in Fig. 4b. In the WT, the shear stress peaks at canopy height and decreases monotonically above and below $z/h = 1$, while in the field, the normalized Reynolds stress remains almost constant up to $z/h = 1.25$, and then decreases. Thus, we do not observe a constant stress layer (Brunet et al. 1994; Raupach et al. 1986) in the WT, although there is a region with reduced slope at $1.2 < z/h < 1.5$, above the region with sharp gradients at $z/h = 1$. The lack of a constant stress layer is most likely a result of streamwise pressure gradients in the facility due to boundary layer growth (as discussed in Sect. 2.2). The normalized rms values of streamwise and wall-normal velocity fluctuations, σ_i/u_*, are presented in Fig. 4c. Both the streamwise and wall-normal component of the field data, especially the streamwise component, exceed those of the WT, with diminishing differences at canopy height. In the laboratory, the normalized normal Reynolds stresses are lower than those in the field, but the correlation between them, the shear stress, is higher. The former trend is in disagreement with that in Poggi et al. (2004) who find that increasing PFAI caused strongly damped normalized rms values inside but also above the canopy. In the present data, e.g., for $z/h = 1$, the WT normal stresses when normalized by the local shear stress are clearly lower than those in the field. Differences in Reynolds number, pressure gradients, and our WT setup, i.e., shear generator and active grid, may contribute to the discrepancies. Poggi et al. (2004), see very little effect of PFAI on the shear stress at and above the canopy height. In the present data, the existence of a streamwise pressure gradient and resulting vertical gradients in shear stress make such a comparison meaningless.

Figure 4d presents the skewness $\langle u_i^3\rangle/\sigma_i^3$, showing similar trends for the field and laboratory data. The wall-normal skewness is negative at canopy height while the streamwise component is positive, indicating a preference for sweeping motions ($u_1 > 0$ and $u_3 < 0$) at $z/h \cong 1$, consistent with Shaw et al. (1983). For the WT data, the skewness changes sign around $z/h = 1.25$, i.e., $\langle u_1^3\rangle/\sigma_1^3$ becomes negative and $\langle u_3^3\rangle/\sigma_3^3$ becomes positive, indicating a preference for ejections ($u_1 < 0$ and $u_3 > 0$). Similar trends have been observed by Brunet et al. (1994). The large PFAI for the CF causes the magnitudes of the skewnesses to be slightly larger than those of the WT model, in accordance with Poggi et al. (2004).

3.2 Spectral characteristics

In this section, we compare the spectral characteristics of the canopy turbulence in the field to that of the WT measurements at canopy height. We use fast Fourier

transforms to calculate the spatial and temporal spectra. In order to reduce the effects of finite data sets while calculating the spectra, we remove the mean and apply linear detrending with zero padding. We do not use a windowing function. Details on calculating the spectra are provided in Doron et al. (2001) and Nimmo Smith et al. (2005). The spatial spectra presented in this paper are calculated separately for each horizontal line in the 2D vector maps, ensemble averaged, and then averaged over the 11 central lines of the velocity distributions. For the field experiment, the PIV data is used in a twofold manner (R. van Hout et al., submitted for publication). First, the energy at small scales is examined through spatial spectra that can be calculated directly from the instantaneous velocity distributions without the need to use Taylor's "frozen" turbulence hypothesis. Second, invoking Taylor's hypothesis, the PIV data at each point are treated as a time series (f = 4 Hz) to study the energy at large scales. For the WT data only the spatial spectra are calculated since the data do not represent a continuous time series. The energy spectra calculated from the PIV data are compared to spectra calculated from the Sonic Anemometer data (f = 6.9 Hz) in the field and hotwire data in the WT (f = 40 kHz).

An estimation of the dissipation rate, ε, i.e., the energy flux cascading down the inertial range, not to be confused with the total dissipation rate in canopy flows (Finnigan 2000), is obtained by fitting a −5/3 slope line to the spatial PIV spectra, assuming that:

$$E_{11}(\kappa_1) = (18/55)C_\kappa \varepsilon^{2/3}\kappa_1^{-5/3} \tag{1}$$

and using $C_\kappa = 1.6$, where κ_1 is the longitudinal wavenumber. This approach assumes that an inertial subrange with a −5/3 slope exists. However, Finnigan (2000) argues that direct interactions between either mean flow or turbulence with canopy elements modify/bypass the cascading process, transferring energy from all scales directly to the dissipation range. Consequently, the spectra are modified. Finnigan (2000) introduces a modified Kolmogorov theory that accounts for this bypass while estimating the energy cascading component. He concludes that the use of the standard Kolmogorov expression overestimates the eddy cascade energy flux, e.g., for a WT model wheat canopy by about one third, and for data obtained in a forest by 2.5–3 times. These adjustments only apply to turbulence inside the canopy height.

In the present WT data, our resolution is about five Kolmogorov scales, as will be shown shortly. Thus, we can also estimate the dissipation rate directly, denoted as ε^D, from measured velocity gradients, keeping in mind that we are slightly under-resolved (L. Luznik et al., submitted for publication). Since the out-of-plane components are not available, we calculate ε^D, using the in-plane contribution to the dissipation rate and multiply it by 15/7 to account of the out-of-plane contribution, assuming isotropic, homogeneous turbulence (Fincham et al. 1996). The resulting expression is

$$\varepsilon^D = \frac{15}{7}\nu\left[2\left\langle\frac{\partial u_1}{\partial x}^2\right\rangle + 2\left\langle\frac{\partial u_3}{\partial z}^2\right\rangle + \left\langle\frac{\partial u_1}{\partial z}^2\right\rangle + \left\langle\frac{\partial u_3}{\partial x}^2\right\rangle + 2\left\langle\frac{\partial u_1}{\partial z}\frac{\partial u_3}{\partial x}\right\rangle\right]. \tag{2}$$

Table 2 compares the direct estimate, ε^D, to the spectral estimate, ε, for the WT data. As is evident, they are always of the same order and differ by 5–30% without a clear trend. For the CF data, R. van Hout et al. (submitted for publication) compare spectral and subgrid-scale (SGS) energy fluxes for various filter sizes. The SGS energy flux represents the actual energy flux in the inertial range and for homogenous, isotropic turbulence, $\varepsilon^{SGS} = \varepsilon$. In our case, the turbulence is neither homogeneous nor isotropic. The CF SGS energy flux is about 20–40% of ε, consistent with Finnigan's (2000) estimate of the ratio between ε and the cascading energy. We conclude that the present spectral estimate of the dissipation maybe not be highly accurate but it is of the correct order of magnitude. Using this value, the Taylor microscale, λ, at $z/h = 0.97$, estimated from $\varepsilon = 15\nu\, u_1^2/\lambda^2$, is 40 mm in the field and 8 mm in the WT. The corresponding Reynolds numbers, based on the Taylor microscale $R_\lambda = u_1\,\lambda/\nu$, are 2,000 and 800 in the field and WT, respectively.

Combining field and WT PIV measurements enables us to resolve almost six decades in the wavenumber space, covering the $2 \times 10^{-6} < \kappa_1\eta < 1.25$ range as shown in Fig. 5 for $z/h = 0.97$, where η is the Kolmogorov length ($\eta = (\nu^3/\varepsilon)^{1/4}$). η was about 0.4 mm for the field and 0.15 mm for the WT. As is evident, the inertial range extends over three decades, from $\kappa_1\ \eta \cong 10^{-4}$ to 10^{-1} for the field data. However, it shrinks to two decades for the WT spectra due to a lower Reynolds number. For the field data, the PIV time series covers the $2 \times 10^{-6} < \kappa_1\eta < 3 \times 10^{-3}$ range, while the spatial spectra cover $2 \times 10^{-2} < \kappa_1\eta < 3 \times 10^{-1}$. The spectra obtained from the field PIV and sonic anemometer time series are similar. The small discrepancies may be attributed to the slight misalignments, different location and slight differences in height. For the WT data, the hotwire and PIV spectra agree very well except for the high wavenumber, where noise becomes a factor in the PIV data.

3.3 Conditional sampling

In this section, Q-H analysis (Willmarth and Lu 1972; Raupach 1981; W. Zhu et al., submitted for publication) is applied to the PIV data sets and used to conditionally sample the Reynolds shear stress, vorticity magnitude and dissipation rate. The data is divided into four quadrants based on the sign of instantaneous values of velocity fluctuation. In quadrant 1, $u_1 > 0$, $u_3 > 0$, in quadrant 2, $u_1 < 0$, $u_3 > 0$ (ejection), in quadrant 3, $u_1 < 0$, $u_3 < 0$, and in quadrant 4, $u_1 > 0$, $u_3 < 0$ (sweep). The bases of conditional sampling are the

Table 2 Comparison of dissipation rate estimated by direct calculation, ε^D (Eq. 2), and by a $-5/3$ line fit to the energy spectra, ε, for wind tunnel data

z/h	ε^D(m^2/s^3)	ε (m^2/s^3)
2.13	2.33	1.58
1.96	3.16	2.48
1.78	3.94	3.36
1.61	4.80	5.50
1.43	5.20	6.51
1.26	5.36	7.06
1.10	5.78	6.74
0.96	9.17	9.66
0.81	6.59	5.75

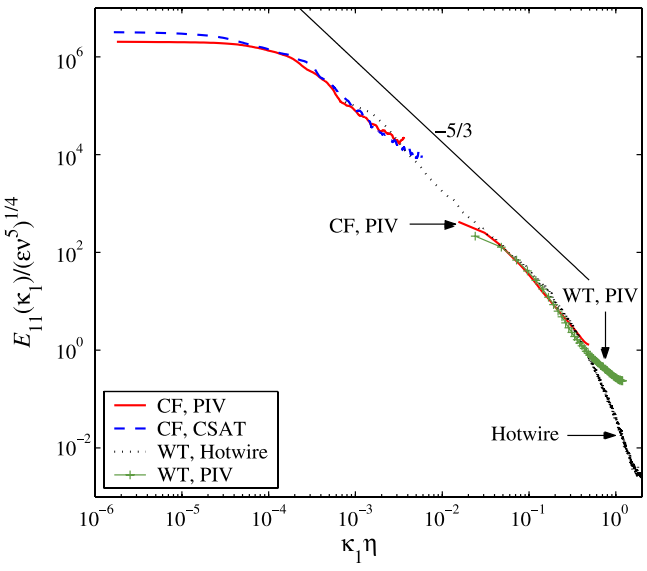

Fig. 5 Normalized longitudinal turbulent kinetic energy spectra at canopy height. *CF* Corn field, *WT* Wind tunnel data

average values of u_1, u_3 and u_1u_3 over the central one third of the vector map. For each quadrant, we conditionally sample the above mentioned parameters based on the magnitude of u_1u_3, the instantaneous shear stress. The trends with elevation of the laboratory and field data are compared. In Q-H analysis, the duration fraction in quadrant k, D_H^k, is defined as the fraction of measurements for which a certain threshold level, H (e.g., based on instantaneous shear stress magnitude), is satisfied:

$$D_H^k = \frac{1}{N}\sum_{n=1}^{N} I_{H,n}^k \tag{3}$$

where the subscript, n, refers to a specific instantaneous value, k is a quadrant number and N is the ensemble size. The parameter, I_H^k, is equal to 1 when the condition is satisfied and $I_H^k = 0$ otherwise. For $H = 0$, the sum of duration fractions of all the four quadrants is 1. The impact of a certain variable, Q, e.g., the Reynolds stress, dissipation, vorticity and production, etc. in each quadrant, is determined by its contribution to the total ensemble averaged value, i.e., by the fraction:

$$\phi_{Q|H}^k = \frac{\langle Q\rangle_H^k}{\langle Q\rangle} D_H^k \tag{4}$$

where $\langle .. \rangle_H^k$ implies averaging of Q over data belonging to quadrant k and exceeding the threshold H. In this paper, the values of H are,

$$H = \frac{\left|(u_1u_3)_{\text{threshold}}\right|}{\left|\langle u_1u_3\rangle\right|} \tag{5}$$

and the analysis examines trends of several parameters conditioned based on H. The stress based duration fraction, D_H^k, and the stress fraction, $\phi_{u_1u_3|H}^k$, are presented in Figs. 6 and 7, respectively. In these and subsequent figures, the WT measurements at $z/h = 0.96$ and 1.26, are compared to field data at $z/h = 0.97$ and 1.29. We also present WT data for $z/h = 0.81$ and 2.13 to examine trends with height. Results are presented only when the number of conditionally sampled instantaneous points exceeds 30. For both field and WT data, the duration fractions of ejection (quadrant 2) and sweep (quadrant 4) events exceed those in quadrants 1 and 3. As expected, D_H^k decreases with increasing H. The overall duration fraction (i.e., $H = 0$) of ejections decreases with height, while the duration of sweeps increases with elevation. Compared to the field results, the WT data contain less extreme events. For example, the WT flow has very few sweeps satisfying $H > 6$, while in the field the $H > 6$ events still have a significant duration fraction. In addition, quadrants 1 and 3 events are extremely rare in the WT, indicating a total dominance of sweep and ejection events. The trends of stress fraction of the two data sets (Fig. 7) compare well in quadrants 1–3, but show conflicting trends in quadrant

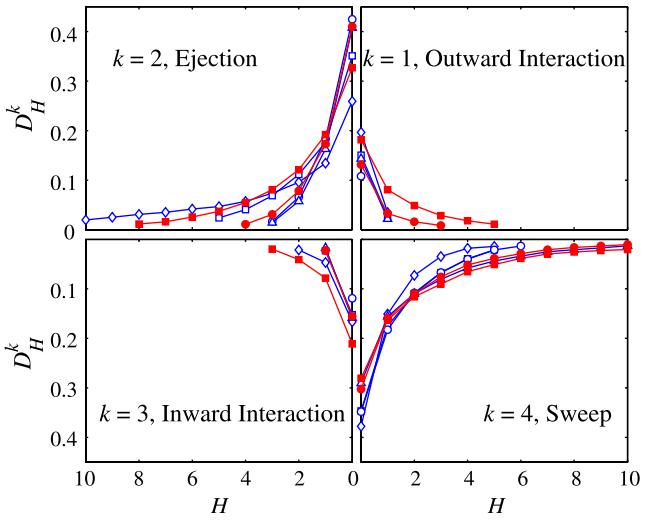

Fig. 6 Duration fraction conditioned on shear stress magnitude for the four quadrants. Wind tunnel: ◇ $z/h = 2.13$, □ $z/h = 1.26$, ○ $z/h = 0.96$, △ $= 0.81$. Corn field ■ $z/h = 1.29$, ● $z/h = 0.97$

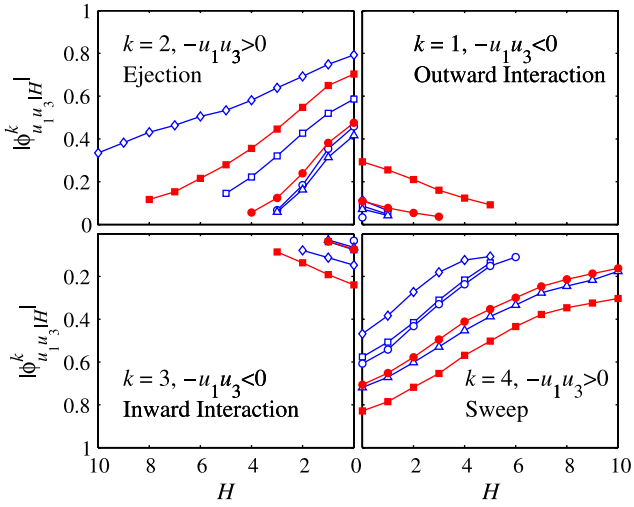

Fig. 7 Conditionally sampled Reynolds stress fractions. For legends see Fig. 6

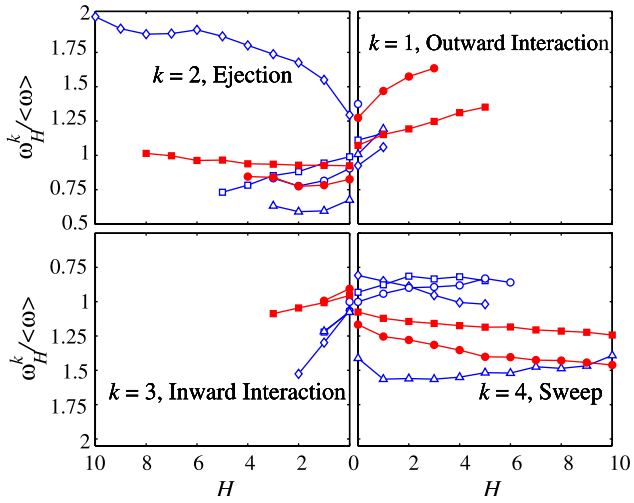

Fig. 8 Vorticity magnitude ratio. For legends see Fig. 6

4. In the WT, the stress fraction in the sweep quadrant decreases with increasing elevation, consistent with Raupach (1981). In the field data, the stress fraction increases with elevation in all four quadrants, with the negative contribution of the first and third quadrants balancing the increasing values in the second and fourth quadrants. These trends are consistent with the CF data of Shaw et al. (1983). Possible reasons for the discrepancy are different Reynolds numbers and roughness densities. Support for the effect of the latter exists in the literature. For example, Raupach (1981) and Poggi et al. (2004) show that the stress fraction difference between sweep and ejection quadrants increases with increasing PFAI inside the layer influenced by the roughness elements. The same trend is obtained when comparing the stress fraction differences of the CF (PFAI = 3.7) to that of the WT (PFAI = 1.0). In the field, the sweep contribution is markedly higher than that of the ejection, while in the WT, they have similar magnitudes.

The conditionally sampled transverse vorticity magnitude, ω_H^k, normalized with its ensemble mean is shown in Fig. 8. Since the PIV resolution does not reach to scales smaller than the Kolmogorov scale, the vorticity is not fully resolved. The vorticity reported in the present analysis thus may underestimate the actual vorticity magnitude by a small factor but the Q-H analysis trends are expected to be realistic. Note that due to differences in the value of vorticity magnitude at different elevations, one should not interpret variation with elevation as trends of vorticity magnitude. In quadrants 2 and 4, the vorticity magnitude does not seem to vary significantly with stress, with the exception of the highest elevation (z/h = 2.13) in quadrant 2. In quadrants 1 and 3, ω increases with H. In addition, for the field data it is evident that when $u_1 > 0$ (quadrants 1 and 4), the quadrant averaged vorticity magnitudes are higher than those occurring when $u_1 < 0$. In the WT, this trend is only true at z/h = 0.81.

The normalized conditionally sampled dissipation rate, $\varepsilon_H^k(z)/\varepsilon(z)$, is shown in Fig. 9. The ensemble averaged dissipation $\varepsilon(z)$ and conditionally sampled dissipation $\varepsilon_H^k(z)$ at certain elevation z are estimated using the same procedures as described in Sect. 3.2. As shown in W. Zhu et al. (submitted for publication), the conditionally sampled spectra maintain the same shape, but shift up or down as ε_H^k varies. The results show similar trends to those of the normalized vorticity, due to the high correlation between vorticity and dissipation rate (Tennekes and Lumley 1972; Zhu and Antonia 1997; Zeff et al. 2003; W. Zhu et al., submitted for publication). In the ejection quadrant, there is little difference between WT and field data, while in the sweep quadrant the difference increases with increasing H. The same is true for both ω and ε. For the highest elevation in the WT, the vorticity and the dissipation rate of the

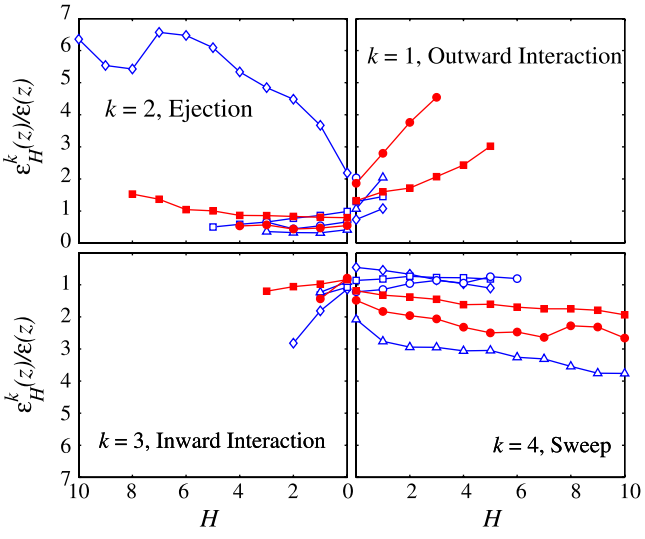

Fig. 9 Normalized dissipation rate. For legends see Fig. 6

ejection events are much higher than their values at other quadrants. The large contribution of ejections to the dissipation fraction at this height is shown in Fig. 10. At this elevation, ejections have the lowest duration fraction (see Fig. 6), but generate almost 60% of the total dissipation rate. Thus, relatively few extreme ejection events are primary contributors to dissipation rate. Previous studies have shown that extreme ejection events contribute substantially to the momentum flux (Willmarth and Lu 1972). Here, we observe a similar trend for the dissipation rate. At the lowest elevation, the trend is reversed, and 60% of the total dissipation rate is generated by sweeps. With increasing elevation, the dissipation rate fraction increases in quadrant 2 and decreases in quadrant 4.

4 Conclusions and discussions

The mean and turbulence flow characteristics inside and above canopies have been measured in a fully-grown CF and in a WT model canopy. The laboratory normalized streamwise mean velocity profile is matched with that of the field data, but the projected LAI is not. The Reynolds shear stress and the rms values of velocity fluctuations peak approximately at canopy height. Their normalized values in the field and WT differ by about 20%, and there is no constant Reynolds shear stress layer in the WT, presumably due to streamwise pressure gradients. The WT vertical skewness profiles show a preference for sweeps below $z/h = 1.25$, and for ejections at higher elevations, as confirmed by Q-H analysis. In the turbulent kinetic energy spectra, the PIV time series resolves large scales, while the spatial PIV spectra resolve small scales. Combining them enables us to resolve almost six decades in wavenumber space, ranging from $2 \times 10^{-6} < \kappa_1\eta < 1.25$. The inertial range of the field data spans three orders of magnitude, and it decreases to two orders for the laboratory data.

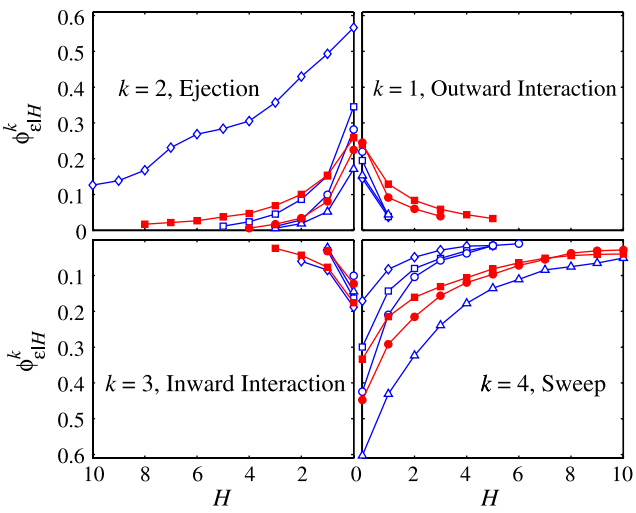

Fig. 10 Dissipation rate fraction. For legends see Fig. 6

Quadrant-Hole analysis examines trends of the Reynolds shear stress, vorticity magnitude and dissipation rate. With the exception of the Reynolds shear stress in the sweep quadrant, these conditionally sampled variables show similar trends with elevation in the WT and in the field. Conversely, in the sweep quadrant the stress fraction of the field data increases with elevation, whereas in the WT decreases with height. This difference is most probably related to the 3.7:1 ratio in PFAI, i.e., the roughness density, consistent with studies of Raupach (1981) and Poggi et al. (2004) as discussed before. At approximately twice the canopy height, the WT ejections have significantly larger stress and dissipation fraction compared to the other quadrants. In contrast, sweep events dominate near canopy height.

In addition to roughness density, there are other issues that one could raise regarding the present comparisons. The influence of waving motion that occurs in real crops, e.g., wheat, as discussed by Finnigan (1979), is not modeled in the WT setup. However, corn stems are actually rather stiff (Goodman and Ennos 1999), and during our experiments we did not observe significant waving motion of the plants at the measured wind speeds. Furthermore, several other studies performed in real corn canopies (Shaw et al. 1974a, 1974b; Wilson et al. 1982) also do not report waving motion.

In both field and WT, a crude estimate of the eddy cascade energy flux is obtained using a $-5/3$ slope line fit to the longitudinal turbulent kinetic energy spectra, assuming local isotropy. However, according to Finnigan (2000), this approach overestimates the cascading energy due to additional mechanisms that convert mean and turbulent kinetic energy directly to dissipation scales. For the WT data, the spectral estimate is within 30% of values calculated directly from the slightly under-resolved instantaneous strain rates. For the CF data, the SGS energy flux which represents the actual eddy cascade energy flux is about 20–40% of the spectral estimate at various filter sizes. Thus, the present spectral estimates are of the correct order of magnitude and we expect that our dissipation estimates provide the correct trends with elevation as well as for conditional sampling.

The field and WT measurements can be improved in a number of aspects. In our experiment only the streamwise and the wall-normal velocities are measured. The velocity distribution in the spanwise direction can be obtained by slightly altering the experimental setup. In addition, we do not resolve the spatial heterogeneity of the flow within the canopy, which is supposedly very severe in the front and rear zone of each canopy element. Furthermore, to resolve the larger scale flow structure, a larger camera's field of view should be employed. Nevertheless, as the first attempt to explore the application of PIV both in field and WT canopy flow, we hope that this study promotes the promising opportunity of this technique in canopy flows.

Acknowledgments We would like to thank Mike Embry of the Wye Research and Education Center of the University of Maryland for

his help in finding a proper location to conduct the field experiments, and Mac Farms Inc., for generously granting us access to their corn field. We are also grateful to Y. Ronzhes and S. King for their technical expertise in developing and maintaining the equipment, as well as J. Kleissl and M. Parlange for providing us with the sonic anemometer data. This research was funded by the Bio-Complexity Program of the National Science Foundation under grant 0119903. The experiments presented in this paper comply with the current laws of the country in which they were performed.

References

Brunet Y, Finnigan JJ, Raupach MR (1994) A wind tunnel study of air flow in waving wheat: single point velocity statistics. Bound-Layer Meteorol 70:95–132

Fincham AM, Maxworthy T, Spedding GR (1996) Energy dissipation and vortex structure in freely decaying, stratified grid turbulence. Dyn Atmos Oceans 23:155–169

Finnigan JJ (1979) Turbulence in waving wheat. I. Mean statistics and honami. Bound-Layer Meteorol 16:181–211

Finnigan JJ (2000) Turbulence in plant canopies. Annu Rev Fluid Mech 32:519–571

Goodman AM, Ennos AR (1999) The effects of soil bulk density on the morphology and anchorage mechanics of the root systems of sunflower and maize. Ann Bot 83:293–302

Jacobson MZ (1999) Fundamentals of atmospheric modeling. Cambridge University Press, 205 pp

Kang HS, Chester S, Meneveau C (2003) Decaying turbulence in an active-grid-generated flow and comparisons with large-eddy simulation. J Fluid Mech 480:129–160

Karnik U, Tavoularis S (1987) Generation and manipulation of uniform shear with the use of screens. Exp Fluids 5:247–254

Nimmo Smith WAM, Atsavapranee P, Katz J, Osborn TR (2002) PIV measurements in the bottom boundary layer of the coastal ocean. Exp Fluids 33:962–971

Nimmo Smith WAM, Katz J, Osborn TR (2005) On the structure of turbulence in the bottom boundary layer of the coastal ocean. J Phys Oceanogr 35:72–93

Poggi D, Porporato A, Ridolfi L, Albertson JD, Katul GG (2004) The effect of vegetation density on canopy sub-layer turbulence. Bound-layer Meteorol 111:565–587

Raupach MR (1981) Conditional statistics of Reynolds stress in rough-wall and smooth-wall turbulent boundary layers. J Fluid Mech 108:363–382

Raupach MR, Antonia RA, Rajagopalan S (1991) Rough-wall turbulent boundary layers. Appl Mech Rev 44:1–25

Roth GI, Katz J (1999) Parallel truncated multiplication and other methods for improving the speed and accuracy of PIV calculations. Proceedings of the 3rd ASME/JSME joint fluids engineering conference, July 18–23, San Francisco

Roth GI, Katz J (2001) Five techniques for increasing the speed and accuracy of PIV interrogation. Meas Sci Technol 16:1568–1579

Shaw RH, Silversides RH, Thurtell GW (1974a) Some observations of turbulence and turbulent transport within and above plant canopies. Bound-Layer Meteorol 5:429–449

Shaw RH, Den Hartog G, King KM, Thurtell GW (1974b) Measurements of mean wind flow and three-dimensional turbulence intensity within a mature corn canopy. Agric Meteorol 13:419–425

Shaw RH, Tavangar J, Ward DP (1983) Structure of the Reynolds stress in a canopy layer. J Clim Appl Meteorol 22:1922–1931

Tennekes H, Lumley JL (1972) A first course in turbulence. MIT, Cambridge, 88 pp

Willmarth WW, Lu SS (1972) Structure of the Reynolds stress near the wall. J Fluid Mech 55:65–92

Wilson JD, Ward DP, Thurtell GW, Kidd GE (1982) Statistics of atmospheric turbulence within and above a corn canopy. Bound-Layer Meteorol 24:495–519

Zeff BW, Lanterman DD, McAllister R, Roy R, Kostelich EJ, Lathrop DP (2003) Measuring intense rotation and dissipation in turbulent flows. Nature 421:146–149

Zhu Y, Antonia RA (1997) On the correlation between enstrophy and energy dissipation rate in a turbulent wake. Appl Sci Res 57:337–347